Chiral Hausdorff metrics and structural spectroscopy in a complex system

Chiral Hausdorff metrics and structural spectroscopy in a complex system

L Coffey†, J A Drapala† and T Erber†‡

† Department of Physics, Illinois Institute of Technology, Chicago, IL 60616, USA
‡ Department of Computer Science and Applied Mathematics, Illinois Institute of Technology, Chicago, IL 60616, USA

Abstract. The surface Coulomb problem consists of finding the locally stable equilibrium configurations of N equal charges confined to the surface of a sphere. In the range $2 \leqslant N \leqslant 112$, computer searches have located 2054 equilibrium states including 1824 that occur in chiral pairs. The structural difference between the 'left' and the 'right' partners of each pair, i.e. the degree of chiral symmetry breaking, can be described in quantitative terms by computing the Hausdorff distance between the two enantiomorphic configurations. The results show that there is a general, albeit not universal, correlation between increasing complexity, decreasing symmetry, and increasing Hausdorff distance. The distribution of distances generated by the relative rotations of the pairs yield an intrinsic characterization of their shapes. The orientations with minimum distances, or optimum overlap, lead to reptation transforms that provide upper bounds for the saddle point heights separating the chiral minima on the energy surfaces. Since the Hausdorff metric constructions are generally asymmetric, the 'left' → 'right' and 'right' → 'left' distances may differ. These distinctions are related to classical parity violation and Hilbert's thirteenth problem.

1. Introduction

Many symmetries of physical systems are of interest because of their dichotomic 'all-or-nothing' character. For instance, all rigid geometric figures can be sorted into non-chiral or chiral classes depending on whether or not they can be rotated into coincidence with their mirror images. In group theoretical terms this simply means that all isometric transformations are either proper or improper—there are no intermediate choices. At the next level of refinement, it is often useful to introduce continuous measures that provide a quantitative scale indicating the extent to which a symmetry is broken. For instance, parity violation in β decay is a direct consequence of the asymmetry in the direction of electron emission relative to the nuclear spin; but the observation that this asymmetry parameter is as large as possible also '...points to something even more drastic and significant' [1]. Similarly, in hadron physics, the standard QCD Hamiltonian includes a term that violates isospin symmetry: the importance of its effects in perturbation expansions is determined by a symmetry-breaking parameter proportional to the quark mass difference $m_d - m_u$ [2].

Chiral symmetries are also essential elements of stereochemistry and crystallography. In these contexts the motivation for assigning a ranking or measure to the chirality of molecules or crystals originated from correlations between optical rotatory power and structural asymmetries [3–5]. However, even after the accumulation of a century of data and analyses for a great variety of systems, the construction of useful chirality measures still remains an unresolved issue [6–9].

In a recent review, Mislow and collaborators pointed out that the Hausdorff distance between sets could be adapted to quantifying the differences between a chiral object and its mirror image [10]. They illustrated the computational viability of this approach by constructing optimally chiral triangles and tetrahedra. A convenient 'test-bed' of much greater complexity is provided by the equilibrium configurations of N equal charges confined to the surface of a sphere.

Extensive computer searches, spanning the range $2 \leqslant N \leqslant 112$, have identified 2054 locally stable states, of which 1824 occur in chiral pairs [11, 12]. These Coulomb states display a rich variety of chiral structures ranging from simple ordered patterns at $N = 15, 16, 23, \ldots$, to highly asymmetric, but non-random, configurations for larger values of N. Typically, for $N \geqslant 80$, the charge distributions become so irregular that there is practically no overlap with any of the standard crystallographic symmetry classes [13]. Detecting the latent elements of order in these complicated structures requires new kinds of indices such as the angular diversity ratios and dipole moments introduced in [11, 12]; and—by fortunate coincidence—the rankings generated by the Hausdorff–Mislow metric. This connection was in fact already anticipated in [10] by the general conjecture that geometric figures with the least symmetry would also have the greatest chirality. A numerical survey extending over the entire Coulomb 'test-bed' confirms this trend: chiral pairs of charge distributions separated by large Hausdorff distances also tend to have irregular structures. However, even for the largest values of N there are some conspicuous fluctuations in the distances. These are associated with particular chiral pairs that have at least one mutual orientation where the two charge distributions nearly coincide. This sensitive correlation between the Hausdorff distances and the particle configurations is useful in other applications that are not restricted to chiral symmetry.

Because the Coulomb configurations are restricted to the surface of a sphere, it is computationally feasible with workstations to determine all of the Hausdorff distances between sets of charges when their relative orientations are varied in $1°$ steps: with three rotational degrees of freedom these gyrations sample about 2.3×10^7 distinct positions. This procedure yields good approximations for the minimum distances and also leads to statistical distributions that specify the number of relative orientations corresponding to any particular value of the Hausdorff distance. Numerical trials show that the variations of these distance distributions reflect spatial conformations of the charge sets, and in this sense are equivalent to a 'structural spectroscopy'.

The special orientations associated with the minimum Hausdorff distances between two Coulomb sets—say A and B—approximate the maximum overlap of the two configurations. Quantitatively this means that the spherical distances between every charge in A and the nearest-neighbour charges in B are as small as possible. Since the A and B configurations correspond to local minima on a multidimensional Coulomb 'energy landscape', it is plausible that the lowest saddle point separating the A and B minima lies on a path between the states of maximum overlap. Starting from this constraint, a numerical sampling of the profiles of these paths is also feasible, and leads to upper bound estimates of the energy barrier height separating chiral states.

A crucial feature of the Hausdorff metric is that the construction of the distance between two sets A and B generally leads to asymmetric results. In particular, even if A and B are identified with chiral pairs of Coulomb configurations, it can be shown that there are mutual orientations where the distance from A to B is not necessarily equal to the distance from B to A. Of course, this asymmetry does not affect the intrinsic arbitrariness of the choice of labels: the set A may be designated as the 'left' enantiomorph and B its 'right' reflected image, or vice versa [14]. But this latitude does not exclude the possibility of distinguishing 'left-A' from 'right-B' because the A to B Hausdorff distance may be larger than the B to A distance. Furthermore, since the Hausdorff distances between finite sets of points are invariant under

reflection, the direction of the distance inequality—e.g. '*A* to *B*' larger than '*B* to *A*'—is also preserved under reflection. Accordingly, these metric constructions are examples of situations where the conventional presumptions concerning the complete equivalence of chiral 'left' and 'right' configurations are not satisfied [15]. In cases where the Hausdorff distances may be identified with physical observables—such as optical rotation—these asymmetries are related to the origin of parity-violating effects.

2. Hausdorff metrics for the surface Coulomb configurations

The Hausdorff distance between two sets *A* and *B* is the smallest number $\delta(A, B)$ satisfying two conditions: (i) a spherical ball with radius δ centred at any point of *A* contains at least one point of *B*; and conversely (ii) a spherical ball of radius δ centred at any point of *B* contains at least one point of *A* [10, 16]. The essential purpose of this dual overlap construction is to ensure that δ satisfies all the criteria for a metric [17]. In particular, if *C* is another bounded set, then the three Hausdorff distances are constrained by the triangle inequality: $\delta(A, C) + \delta(C, B) \geqslant \delta(A, B)$. Since *A* and *B* are usually considered to be compact subsets of a complete metric space with a metric *m*—thereby assigning quantitative meaning to the radii of spherical balls—the Hausdorff distance δ may be regarded as a 'collective measure' that is superposed on the underlying *m*-metric.

Specializing this metric construction to the Coulomb states is straightforward. Let $C^L(\vec{r}_1, \ldots, \vec{r}_i, \ldots, \vec{r}_N)$ denote a chiral state specified by a set of radial vectors, $|\vec{r}_i| = 1$, that locate the *N* point charges on the surface of a unit sphere. Similarly, let $C^R(\vec{r}_1, \ldots, \vec{r}_i, \ldots, \vec{r}_N)$ denote its enantiomorphic partner. Furthermore, suppose that the 2*N* charges of C^L and C^R are simultaneously placed on the sphere. Then the angular separations between all pairings of 'unlike' charges—one each from C^L and C^R—are given by the set of N^2 angles Ψ_{ij} where

$$\Psi_{ij} = \cos^{-1}(\vec{r}_i \cdot \vec{r}_j), \ldots, 1 \leqslant i, j \leqslant N. \tag{1}$$

It is convenient to list these angles in the format of a square array:

$$
\begin{array}{ccccccccc}
\Psi_{11} & \Psi_{12} & . & . & . & \Psi_{18} & . & . & . & \Psi_{1N} \\
. & . & . & . & . & . & . & . & . \\
. & . & . & . & . & . & . & . & . \\
\Psi_{i1} & \Psi_{i2} & . & . & . & \Psi_{ij} & . & . & . & \Psi_{iN} \\
. & . & . & . & . & . & . & . & . \\
. & . & . & . & . & . & . & . & . \\
\Psi_{N1} & \Psi_{N2} & . & . & . & \Psi_{Nj} & . & . & . & \Psi_{NN}.
\end{array} \tag{2}
$$

Suppose, for illustration, that Ψ_{18} happens to be the smallest angle in the first row, i.e. $\Psi_{18} = \min_j \Psi_{1j}$. This means that Ψ_{18} is the angular radius of the smallest spherical cap centred at $\vec{r}_1$—the position of the first charge in C^L—that also includes at least one charge, in this case the eighth, belonging to C^R. Similar minimal disc radii ($\min_j \Psi_{ij}$) appear in all the other rows of the array. The largest angle among this set of minima

$$\max_i \min_j \Psi_{ij} = \delta(C^L \to C^R) \tag{3}$$

then evidently corresponds to the first part of the Hausdorff distance construction adapted to configurations of points on the spherical surface S^2. Specifically, equation (3) delimits the angular radius of the smallest closed spherical cap $s \subset S^2$ with the property that whenever *s* is centred on any of the C^L charges, at least one C^R charge is contained in *s*. As indicated by the notation, (3) corresponds to a 'C^L to C^R' distance.

The second part of the Hausdorff distance construction follows simply by replacing the max–min by-rows algorithm in equation (3) by a complementary max–min by-columns algorithm, namely:

$$\max_{j} \min_{i} \Psi_{ij} = \delta(C^R \rightarrow C^L). \tag{4}$$

It is easy to verify that the structure of the array in (2) ensures that (4) yields the angular radius of the smallest spherical cap $\bar{s}$ with the property that whenever $\bar{s}$ is centred on any of the C^R charges, at least one C^L charge is contained in $\bar{s}$. Since, in general, $\vec{r}_i \cdot \vec{r}_j \neq \vec{r}_j \cdot \vec{r}_i$, the array in (2) is not necessarily symmetric ($\Psi_{ij} \neq \Psi_{ji}$), and therefore the max–min values located by the row and column searches in (3) and (4) may be different. In such cases the directed Hausdorff distances, $\delta(C^L \rightarrow C^R)$ and $\delta(C^R \rightarrow C^L)$, may be unequal even though the underlying m-metric is symmetric.

Finally, (3) and (4) may be combined to yield the standard Hausdorff distance between sets C^L and C^R:

$$\delta(C^L, C^R) = \max[\delta(C^L \rightarrow C^R), \delta(C^R \rightarrow C^L)]. \tag{5}$$

This expression is obviously symmetric in C^L and C^R, and satisfies all the other criteria for a metric including the triangle inequality [16]. Of course, the distances determined by (3)–(5) also depend on the relative orientations of the sets C^L and C^R. Therefore, minimizing with respect to the remaining degrees of freedom of the rotation group O_3, yields minimum Hausdorff distances between C^L and C^R. In particular, equation (3) implies that the minimum directed Hausdorff distance from C^L to C^R is given by

$$\delta_{min}(C^L \rightarrow C^R) = \min_{O_3} \max_{i} \min_{j} \Psi_{ij} \tag{6}$$

and similarly from (4) and (5)

$$\delta_{min}(C^R \rightarrow C^L) = \min_{O_3} \delta(C^R \rightarrow C^L); \quad \delta_{min}(C^L, C^R) = \min_{O_3} \delta(C^L, C^R). \tag{7}$$

In practice, these rotational minimizations are implemented by recomputing the basic array of angles in (2) for a large sample of relative orientations of C^L and C^R.

The Hausdorff distances between Coulomb states consisting of N charges placed on the unit sphere are inversely related to N, i.e. $\delta \simeq N^{-1/2}$, because the surface charge densities are $O(4\pi/N)$, and this estimate bounds all characteristic angles—including the Ψ_{ij} in (2)—by $O(N^{-1/2})$. In order to separate these density variations from the chirality rankings it is expedient to rescale the Hausdorff metrics by a 'running' normalization factor. Let $C((\vec{r}_l)_1^N)$ denote any N-particle Coulomb configuration, and $\vec{R}_P$ the position of an arbitrary additional point P on the surface of the unit sphere. Then

$$\Psi_{max} = \max_{\forall \vec{R}_P} \min_{l} \cos^{-1}(\vec{r}_l \cdot \vec{R}_P) \tag{8}$$

is the largest possible angle between a point P located anywhere on the sphere and the nearest charge in C. Clearly, for any particular chiral pair, $\psi_{max}(C^L) = \Psi_{max}(C^R)$. The appropriate set of Hausdorff–Mislow metrics is then obtained by normalizing all the equations (3)–(7), e.g.,

$$d(C^L \rightarrow C^R) = \delta(C^L \rightarrow C^R)/\Psi_{max} \tag{9}$$

$$d(C^L, C^R) = \delta(C^L, C^R)/\Psi_{max} \tag{10}$$

$$d_{min}(C^L, C^R) = \delta_{min}(C^L, C^R)/\Psi_{max} \tag{11}$$

(here and in the succeeding, d designates the normalized distances). Obviously, these divisions remove the $N^{-1/2}$ scaling; and they have the nice additional feature that $0 \leqslant d(C^L, C^R) \leqslant 1$, where 0 means no chirality and 1 denotes maximum chirality.

Table 1. Values of the normalizing angle Ψ_{max} for the Hausdorff metrics.

N	E	Ψ_{max}	N	E	Ψ_{max}
12	49.165 25	0.652	58	1438.618 25	0.306
15	80.670 24	0.616	58	1438.625 51	0.316
16	92.911 66	0.581	58	1438.626 29	0.318
23	203.930 19	0.491	58	1438.627 22	0.328
24	223.347 07	0.532	·	·	·
26	265.133 33	0.474	74	2387.072 98	0.280
27	287.309 61	0.466	74	2387.075 17	0.292
28	310.491 54	0.439	74	2387.079 93	0.278
30	359.603 94	0.439	·	·	·
29	334.634 44	0.458	74	2387.087 29	0.296
30	359.603 94	0.439	·	·	·
·	·	·	88	3416.720 19	0.249
·	·	·	88	3416.732 89	0.247
·	·	·	88	3416.772 58	0.252
·	·	·	88	3416.776 26	0.259
47	927.059 27	0.376	·	·	·
47	927.062 27	0.374	·	·	·
47	927.088 23	0.359	·	·	·
47	927.141 09	0.344	100	4448.350 63	0.245
·	·	·	·	·	·
·	·	·	112	5618.044 88	0.215

3. Computations of the Hausdorff metrics

The numerical values of the angles in the basic array (2) can be obtained from the individual charge positions. Following the conventions of [12] these are specified by the spherical colatitude ϕ, $0 \leqslant \phi \leqslant \pi$, and the longitude θ, $-\pi \leqslant \theta \leqslant \pi$. It is then easy to check that the angular separation between the ith and the jth charges is given by

$$\Psi_{ij} = \cos^{-1}(\sin\phi_i \sin\phi_j[\cos(\theta_i - \theta_j) - 1] + \cos(\phi_i - \phi_j)). \tag{12}$$

The normalizing angle Ψ_{max} (8) can be obtained by similar means. In practice, placing a point P anywhere on the sphere $(\forall \vec{R}_P)$ is approximated by stepping through the ranges of ϕ and θ in $1°$ intervals; this covers the sphere with a non-uniform grid of $180 \times 360 = 64\,800$ points. Locating the largest values of $\min_l \cos^{-1}(\vec{r}_l \cdot \vec{R}_P)$ on this grid for all 2054 Coulomb states requires about 10^4 minutes of CPU time on a SGI Indy workstation. Some representative values of Ψ_{max} are listed in table 1. The first column indicates the number of charges N. The next column shows the energy of the configurations—a necessary distinction when multiple chiral pairs occur for a particular N. Finally, the third column lists the corresponding values of Ψ_{max} in radians. The numerical accuracy can be gauged by comparison with the exact results for the icosahedron:

$$\Psi_{max}(12) = \sin^{-1}[(\tfrac{2}{3}[1 - 5^{-1/2}])^{1/2}] \simeq 0.652\,358\,14 \tag{13}$$

and [18]

$$E(12) = 3 + \tfrac{15}{2}([10 - 2\sqrt{5}]^{1/2} + [10 + 2\sqrt{5}]^{1/2}) \simeq 49.165\,253\,05. \tag{14}$$

The overall trend of the results, $\Psi_{max}(N) \simeq N^{-1/2}$, is of course consistent with the normalizations introduced in equations (9)–(11), etc.

It is convenient to begin the Hausdorff distance calculations by considering the special case $\delta(C_s^L, C_s^R)$, where all the charges of both chiral pairs have the standard positions set up

Table 2. Angular coordinates in radians of the 'left' and 'right' Coulomb states for $N = 15$ in standard position.

$C_S^L(\vec{r}_1(\phi_1^L, \theta_1^L), \ldots, \vec{r}_{15}(\phi_{15}^L, \theta_{15}^L))$				$C_S^R(\vec{r}_1(\phi_1^R, \theta_1^R), \ldots, \vec{r}_{15}(\phi_{15}^R, \theta_{15}^R))$			
Charge number i	Colatitude ϕ_i^L	Longitude θ_i^L	Partial energy	Charge number j	Colatitude ϕ_j^R	Longitude θ_j^R	Partial energy
1	0	0	5.333 55	1	0	0	5.333 55
2	2.094	0	5.333 55	2	2.094	0	5.333 55
3	2.094	3.142	5.333 55	3	2.094	−3.142	5.333 55
4	1.792	2.129	5.384 08	4	1.915	−1.074	5.384 08
5	1.915	−2.068	5.384 08	5	1.915	2.068	5.384 08
6	1.792	−1.012	5.384 08	6	0.979	1.653	5.384 08
7	0.979	1.489	5.384 08	7	1.792	−2.129	5.384 08
8	1.915	1.074	5.384 08	8	0.979	−1.489	5.384 08
9	0.979	−1.653	5.384 08	9	1.792	1.012	5.384 08
10	2.712	−1.354	5.394 19	10	1.010	−2.640	5.394 19
11	1.010	2.640	5.394 19	11	1.010	0.501	5.394 19
12	2.712	1.787	5.394 19	12	2.712	1.354	5.394 19
13	1.184	−2.687	5.394 19	13	2.712	−1.787	5.394 19
14	1.010	−0.501	5.394 19	14	1.184	−0.455	5.394 19
15	1.184	0.455	5.394 19	15	1.184	2.687	5.394 19

in [12]. In these orientations, the vectors $\vec{r}_1(\phi_1^L, \theta_1^L)$ and $\vec{r}_1(\phi_1^R, \theta_1^R)$, which locate the charges with the least partial energies, both point to the 'north pole', i.e., $\phi_1^L = \phi_1^R = 0$. The charges with the next higher partial energies $\vec{r}_2(\phi_2^L, \theta_2^L)$ and $\vec{r}_2(\phi_2^R, \theta_2^R)$ are positioned so that they are placed at zero longitude, $\theta_2^L = \theta_2^R = 0$. These conventions—which are explained in detail in section 2B of [12]—eliminate the rotational degeneracies that would otherwise occur in orienting the Coulomb configurations on the sphere. Table 2 displays these standard charge positions for the special case $N = 15$. This is the smallest value of N for which the stable equilibrium configurations of the surface Coulomb problem consist of an enantiomorphic pair of states. These systems are comprised of five parallel rings each containing three charges: the three charges with the lowest partial energies ($i = 1, 2, 3$ and $j = 1, 2, 3$ in table 2) form equilateral triangles around a great circle. The other four triangles are obtained by imparting a twist to the successive rings. Since these twists can be made either in a clockwise or an anticlockwise direction, the resulting pair of configurations cannot be superposed by rotations or proper isometries [12, 19].

The basic angular array (2) can now be obtained by repeated application of (12). When both charge configurations are in the standard positions—where $\vec{r}_1(\phi_1^L, \theta_1^L)$ and $\vec{r}_1(\phi_1^R, \theta_1^R)$ both point to the 'north pole'—it is trivial to verify from (1) that $\Psi_{11} = \cos^{-1}(\vec{r}_1 \cdot \vec{r}_1)$ vanishes identically. But, of course, the other diagonal terms, e.g. Ψ_{ll} for $l > 3$, may have non-zero values. The simple example $\Psi_{34} = \cos^{-1}(\vec{r}_3(2.094, 3.142) \cdot \vec{r}_4(1.915, -1.074)) = 1.792 \neq \Psi_{43} = \cos^{-1}(\vec{r}_4(1.792, 2.129) \cdot \vec{r}_3(2.094, -3.142)) = 0.979$, shows that in general $\Psi_{ij} \neq \Psi_{ji}$. Table 3 lists all of the $N^2 = 225$ angular distances between all pairings of charges from $C_S^L(15)$ and $C_S^R(15)$. The same indexing conventions for numbering the individual charges—i for charges in $C_S^L(15)$ and j for charges in $C_S^R(15)$—are used in tables 2 and 3. For clarity, the table entries are rounded to four significant figures: these results are extracted from more complete computations utilizing angular coordinates for the Coulomb configurations which are accurate to at least seven significant digits [12].

Table 3. Angular array for determining the Hausdorff distance between the two chiral Coulomb states for $N = 15$. Both states are aligned in the standard positions described in the text. Table entries are in radians.

								j							
i	1	2	3	4	5	6	7	8	9	10	11	12	13	14	15
1	<u>0.000</u>	2.094	2.094	1.915	1.915	0.979	1.792	0.979	1.792	1.010	1.010	2.712	2.712	1.184	1.184
2	2.094	<u>0.000</u>	2.094	0.979	1.792	1.915	1.915	1.792	0.979	2.712	1.184	1.010	1.184	1.010	2.712
3	2.094	2.094	<u>0.000</u>	1.792	0.979	1.792	0.979	1.915	1.915	1.184	2.712	1.184	1.010	2.712	1.010
4	1.792	1.915	0.979	2.572	<u>0.136</u>	0.931	1.948	2.572	1.087	1.640	1.736	1.059	1.661	2.586	0.818
5	1.915	1.792	0.979	0.931	1.948	2.572	<u>0.136</u>	1.087	2.572	1.059	2.586	1.640	0.818	1.736	1.661
6	1.792	0.979	1.915	<u>0.136</u>	2.572	2.572	1.087	0.931	1.948	1.736	1.640	1.661	1.059	0.818	2.586
7	0.979	1.792	1.915	2.572	1.087	<u>0.136</u>	2.572	1.948	0.931	1.661	0.818	1.736	2.586	1.640	1.059
8	1.915	0.979	1.792	1.948	0.931	1.087	2.572	2.572	<u>0.136</u>	2.586	1.059	0.818	1.640	1.661	1.736
9	0.979	1.915	1.792	1.087	2.572	1.948	0.931	<u>0.136</u>	2.572	0.818	1.661	2.586	1.736	1.059	1.640
10	2.712	1.010	1.184	0.818	1.640	2.586	1.059	1.736	1.661	1.966	2.193	0.838	<u>0.179</u>	1.674	2.193
11	1.010	2.712	1.184	2.586	1.059	0.818	1.640	1.661	1.736	0.838	1.674	1.966	2.193	2.193	<u>0.179</u>
12	2.172	1.184	1.010	1.640	0.818	1.736	1.661	2.586	1.059	2.193	1.966	<u>0.179</u>	0.838	2.193	1.674
13	1.184	2.172	1.010	1.736	1.661	1.640	0.818	1.059	2.586	<u>0.179</u>	2.193	2.193	1.674	1.966	0.838
14	1.010	1.184	2.712	1.059	2.586	1.661	1.736	0.818	1.640	1.674	0.838	2.193	1.966	<u>0.179</u>	2.193
15	1.184	1.010	2.712	1.661	1.736	1.059	2.586	1.640	0.818	2.193	<u>0.179</u>	1.674	2.193	0.838	1.966

The simple structure of the angular array in table 3 makes it easy to identify the extremals required for the distance measures in (3) and (4). Evidently the successive minima by rows are given by the underlined entries $\min_j \Psi_{1j} = 0, \min_j \Psi_{2j} = 0, \ldots, \min_j \Psi_{15j} = 0.179$; and therefore the largest angle among this set of minima is given by

$$\max_i \min_j \Psi_{ij} = 0.179 = \delta(C_s^L(15) \to C_s^R(15)) \qquad (15)$$

for all the pairs $(i = 13, j = 10), (15,11), (12,12), (10,13), (14,14)$ and $(11,15)$. As indicated in (3), this angle corresponds to the (un-normalized) Hausdorff distance from $C_s^L(15)$ to $C_s^R(15)$. Since the minima by columns in table 3 also lead to the same set of underlined entries, i.e. $\min_i \Psi_{i1} = 0, \min_i \Psi_{i2} = 0, \ldots, \min_i \Psi_{i15} = 0.179$, it is clear that the complementary Hausdorff distance (4)

$$\max_j \min_i \Psi_{ij} = 0.179 = \delta(C_s^R(15) \to C_s^L(15)) \qquad (16)$$

from $C_s^R(15)$ to $C_s^L(15)$ is also equivalent to the preceding result (15). In this symmetric situation, the standard Hausdorff distance (5) between the sets $C_s^L(15)$ and $C_s^R(15)$—given by the maximum of (15) and (16)—is therefore also equal to

$$\delta(C_s^L(15), C_s^R(15)) = 0.179. \qquad (17)$$

Finally, since table 1 shows that the largest possible value of Ψ is $\Psi_{max} = 0.616$ for $N = 15$, the normalized Hausdorff–Mislow distance between the 'left' and the 'right' chiral states—when both are oriented in the standard position—is given by (cf (10)):

$$d(C_s^L(15), C_s^R(15)) \simeq \frac{0.179}{0.616} = 0.291. \qquad (18)$$

According to this criterion, the spatial disposition of the charges $C_s^L(15)$ and $C_s^R(15)$ is quite different despite the obvious correspondences among the coordinates displayed in table 2.

4. Minimum Hausdorff metrics and structural spectroscopy

The next logical step is to drop the restriction that the chiral states are confined to standard orientations, and to find the minimum possible Hausdorff distance between the $C^L(15)$ and $C^R(15)$ configurations when they are free to rotate relative to each other. In principle this is a straightforward procedure: without loss of generality, one of the states, say $C^L_s(15)$, may be chosen to remain fixed in the standard orientation, while the other, $C^R(15)$, is rigidly revolved and spun through the three angular degrees of freedom of the O_3 rotation group. These reorientations can be carried out by tilting the 'north pole' charge of $C^R(15)$—specifically, the charge labelled $j = 1$ in table 2—from its initial position at colatitude $\phi = 0$, longitude $\theta = 0$, to colatitude α, rotating to longitude β, and then recomputing the associated new coordinates of all the other charges $j = 2, \ldots, 15$, resulting from this rigid rotation. For clarity, note that the β rotations occur about a fixed axis through the north pole, while the α tilts are equivalent to rotations about a succession of horizontal axes. The third degree of freedom can be taken into account by constructing an axis extending from the centre of the sphere to the new location of the reference charge, $j = 1$ at α, β, and then rigidly rotating the entire tilted $C^R(15)$ configuration through an angle γ about this axis. The geometry of these Euler angle rotations is shown in figure 8 of the appendix. The corresponding trigonometric transformations that implement the isometric mappings of all the charge coordinates are also given in the appendix.

   In practice, the tilting of the 'north pole' or reference charge is programmed so that the α and β coordinates successively coincide with every point of the 1° grid previously set up for the Ψ_{max} calculations in (8). At every gridpoint, the corresponding set of chiral distances, (9) and (10), can be obtained by recomputing the angular array (2). In these cases, the individual Ψ_{ij} entries represent the angular separations between the ith charge in the standard C^L_s state and the new positions of the jth charge in the tilted C^R configurations. Computing the entire set of Hausdorff distances on the 1° tilt grid for all 912 chiral pairs in the interval $15 \leqslant N \leqslant 112$ requires two days' CPU time on an SGI workstation.

   The results are summarized in figure 1 and table 4. Obviously, larger values of the normalized Hausdorff distances appear more frequently as N increases. This general trend confirms Mislow's basic conjecture that complex configurations with the least symmetry also have the greatest chirality [10]. Since the angular separations between the nearest-neighbour charges in the Coulomb configurations are scaled by the Coulomb angle $\Theta_C(N)$—cf section 4E.1 and table VIII of [12]—it is plausible that for arbitrary relative orientations of $C^L(N)$ and $C^R(N)$ the most probable value of the normalized Hausdorff distance is of the order of $\Theta_C(N)/2\Psi_{max}(N)$. This estimate may be confirmed by averaging over the 20 chiral pairs that occur for $N = 94$; in this case it is easy to verify that both indices, $\langle\Theta_C(94)\rangle/2\langle\Psi_{max}(94)\rangle = 0.72$ and $\langle d(C^L(94), C^R(94))\rangle = 0.72$, lead to equivalent results. But apart from a general correlation between greater complexity and increasing chiral distances, it is also apparent from figure 1 and table 4 that there are considerable fluctuations. For instance, at $N = 100$ the Hausdorff distances between the 18 chiral pairs vary between 0.089 and 0.799. This sensitive dependence of the Hausdorff distance on the detailed structure of the individual charge configurations contrasts favourably with the insensitive variation of the Coulomb energies: the maximum energy difference among all of the 34 states that occur for $N = 100$ is only about 0.01%.

   The Hausdorff distances listed in table 4 are the minimum values for all chiral pairs $C^L_s(N)$ and $C^R_{grid}(N)$ found when the 'north pole', or reference charge, of $C^R_{grid}(N)$ is successively tilted through 1° intervals of the colatitude α and longitude β. This 1° grid includes $179 \times 360 + 2 = 64\,442$ distinct positions, each yielding a value of $d(C^L_s(N), C^R_{grid}(N))$. The
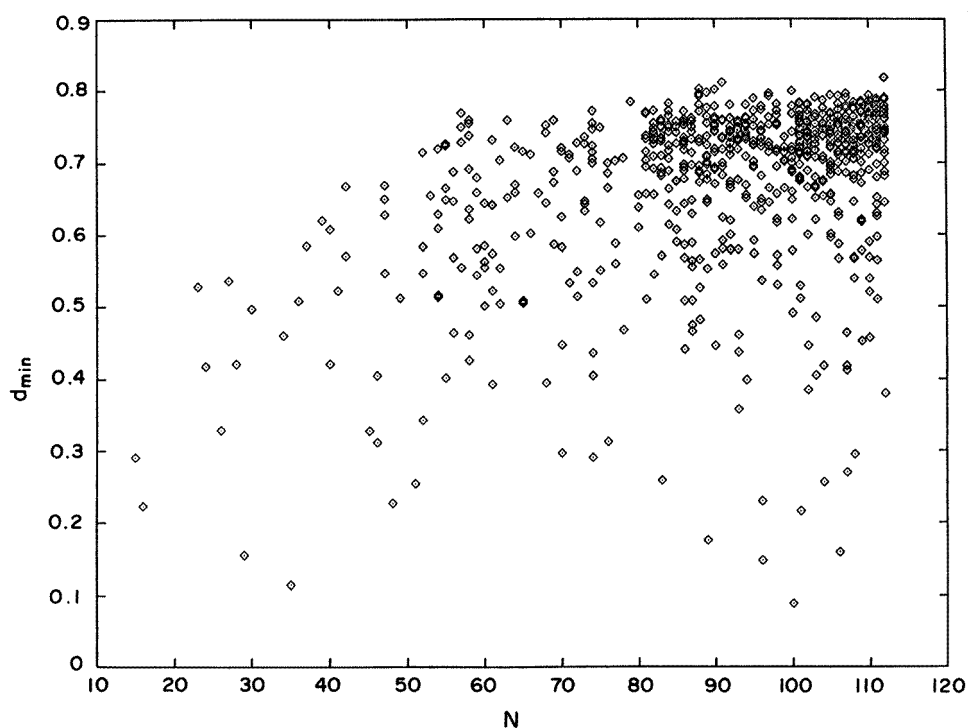
Figure 1. Minimum normalized Hausdorff distance (11) versus the number of charges N for 912 chiral pairs of Coulomb states.

distance entries marked by crosses (+) in table 4 correspond to situations where the minimum values of $d(C_s^L(N), C_{grid}^R(N))$, resulting from grid searches, coincide with $d(C_s^L(N), C_s^R(N))$, the Hausdorff distances between chiral pairs when both configurations are in the standard orientation. These 'standard' distance minima occur for about 8% of all pairs up to $N = 112$. In principle, still lower values of the Hausdorff distances may be located by rotating the tilted $C_{grid}^R(N)$ configurations about the third Euler angle γ shown in figure 8 in the appendix. If these rotations are carried out in $1°$ increments of γ about axes that coincide with every point of the $1°\alpha-\beta$ grid, then the basic angular array in (2) has to be recomputed for a total of about 2.3×10^7 relative rotations of $C_s^L(N)$ and $C^R(N)$. In the particular case of $N = 15$, this comprehensive search yields a minimum Hausdorff distance (cf (11)) of

$$d_{min}(C^L(15), C^R(15)) = \min_{O_3} d(C_s^L(15), C_{grid}^R(15)) = 0.291 \tag{19}$$

which turns out to be no lower than the standard minimum listed in table 4 and equation (18).

Clearly the variations of the Hausdorff distances depend on the relative orientation of pairs of charge configurations as well as the coarseness and distribution of the rotation grids. Consequently the frequency distributions of the Hausdorff distances contain information concerning the intrinsic shapes of the charge structures. In the interest of clarity and consistency this analysis will be illustrated with the non-uniform $1°\alpha-\beta$ grid used in the minimum Hausdorff distance searches, although grids that are uniformly distributed over the sphere are better suited for some purposes. The icosahedron is a convenient illustration of this structural spectroscopy because its symmetries are so well known [20, 21]. Specifically, if $C_s(12)$ denotes an icosahedron in the standard orientation shown in figure 2, and $C_{grid}(12)$ is a copy that is

Table 4. Normalized Hausdorff distances d between chiral pairs of Coulomb states for selected values of N.

N	E	d	N	E	d
15	49.165 25	0.291^+	91	3661.817 98	0.811
16	92.911 66	0.224^+	.	.	.
23	203.930 19	0.528	.	.	.
24	223.347 07	0.418	96	4089.257 54	0.148
26	265.133 33	0.329^+	.	.	.
27	287.309 61	0.536^+	.	.	.
28	310.491 54	0.421	96	4089.258 10	0.773
29	334.634 44	0.156^+	.	.	.
30	359.603 94	0.497	100	4448.447 21	0.089^+
.	.	.	100	4448.489 60	0.799^+
35	498.569 87	0.115	.	.	.
.	.	.	106	5016.053 72	0.159
51	1099.819 29	0.255^+	.	.	.
88	3416.772 59	0.527^+	.	.	.
.	.	.	112	5618.2348	0.817
88	3416.732 91	0.802	112	5618.170 23	0.387
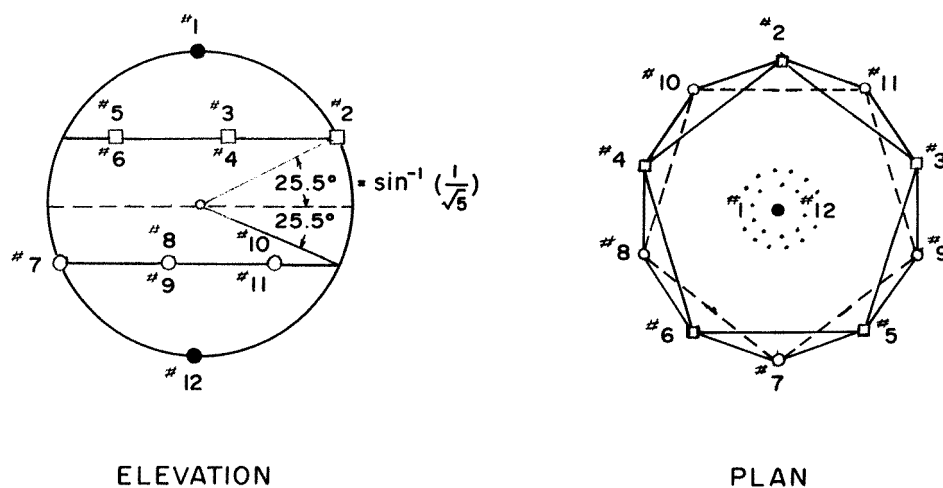
Figure 2. Plan and elevation of an icosahedron. The upper ring of charges (open squares #2–#6) forms a regular pentagon; the lower ring (open circles #7–#11) is another regular pentagon shifted by 36° longitude relative to the upper ring. The central dot in the plan view represents the north (#1) and south (#12) pole charges. The significance of the dotted circles is discussed in the text.

Table 5. Selected values of the Hausdorff distance distribution for the icosahedron. A graph of $F(d)$ covering the entire range $0 \leqslant d \leqslant 1$ is given in figure 3.

d	$F(d)$
0.000	1
0.001	0
.	.
.	.
.	.
0.026	0
0.027	370
0.028	0
.	.
.	.
.	.
0.053	0
0.054	370
0.055	0
.	.
.	.
0.059	20
.	.
.	.
0.855	595
0.856	745
0.857	325
.	.
.	.
0.996	0
0.997	20
0.998	0

rigidly tilted and rotated so that its north pole charge (#1) traverses the $1°\alpha$–β grid, then the top line of table 5 confirms that the Hausdorff distance between the two icosahedra vanishes only when they coincide, i.e. the frequency function F has the value $F(0) = 1$. The first non-trivial entry, $F(0.027) = 370$, results from tilting charge #1 of $C_{grid}(12)$ to colatitude $\alpha = 1°$, and then traversing around the north pole in $1°$ steps of the longitude β—these rotations are represented by the inner dotted circle on the plan view in figure 2. Obviously, these $1°$ off-sets imply that all of the angular distances between nearest-neighbour charges of the two icosahedra are also of the order of $1°$, and therefore the associated normalized Hausdorff distance (cf (13)), $d = 1°/37.377° \simeq 0.0267$, appears 360 times. The ten additional matches result from tilting charge #1 of $C_{grid}(12)$ to colatitude $\alpha = 179°$, near charge #12 at the south pole. This inverted position generally does not lead to a near coincidence of the two icosahedra because their pentagonal rings are offset by $36°$. However it is easy to show with the pentagon models snipped from figure 2, that at the five special longitudes, $\beta = 0°, 72°, 144°, \ldots, 288°$, the ring charges are nearly aligned—allowing for the $1°$ discretization there are in fact ten such positions. Accordingly, for these particular orientations, the Hausdorff distances between the icosahedra also have the minimal value $d \simeq 0.027$. Similar remarks apply to the second increment of tilt $\alpha = 2°$, corresponding to the outer circle of figure 2, and the next entry, $F(0.054) = 370$, in table 5. A graphical summary of the entire Hausdorff distance distribution $F(d)$ is displayed in figure 3. The 0.0267 distance intervals between the prominent spectral
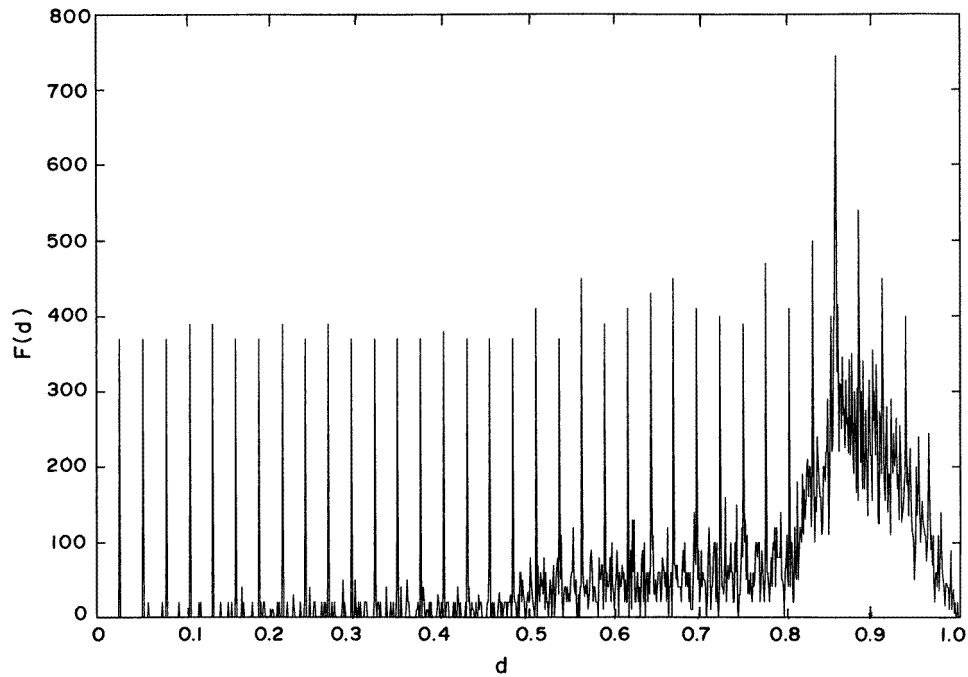
Figure 3. Frequency distribution of the Hausdorff distances for an icosahedron. $F(d)$ is the number of orientations on a spherical latitude–longitude grid with 6.4×10^4 points that yield the same value of the Hausdorff distance d. The 0.0267 spacing between the prominent spectral lines is due to the $1°$ discretization of the grid; the line 'intensities' and other features reflect the structure of the icosahedron.

lines are a direct reflection of the discretization due to the $1°\alpha$–β grid; the heights of the individual lines are determined by the structure of the icosahedron. In particular, the maximum value $F(0.856) = 745$ occurs within 1% of the most probable distance inferred from (13), i.e. $\Theta_C(12)/2\Psi_{max}(12) \simeq 63.434°/2 \times 37.277° \simeq 0.849$. This peak is sharp because it coincides with the 32nd multiple of the line spacing 0.026 75. The last entries in table 5 also have an obvious interpretation. The normalized Hausdorff distances can reach their upper bound ($d \to 1$) only when at least one vertex of $C_{grid}(12)$ approaches one of the maximum $\vec{R}_P$ points found in (8): the icosahedron has exactly 20 of these points—each one centred at a distance of $\simeq 0.205$ above the mid-point of every triangular face.

Figure 4 shows the corresponding results for the chiral pair $C_s^L(15)$ and $C_{grid}^R(15)$. In this case the Hausdorff distance distribution also includes a prominent line spectrum spaced at intervals of $1°/\Psi_{max}(15) \simeq 1°/35.28° \simeq 0.0283$; but, in contrast to the icosahedral distribution, the spectrum begins at $d \simeq 0.291$ because of the lower bounds set by (18) and (19). The sharp increase from $F = 16$ to $F = 82$ at $d \simeq 0.697$ occurs when the normalized Hausdorff distances become comparable to the smallest characteristic length associated with the $C^{L,R}(15)$ states, i.e. $\Theta_c(15)/2\Psi_{max}(15) \simeq 49.22°/2 \times 35.28° \simeq 0.697$. Beyond this threshold, the spectrum reflects the quasi-regular structure of the chiral configurations. Specifically, the five triangular rings that make up $C^{L,R}(15)$ correspond to 'Coulomb' polyhedra [12] with 39 edges grouped into seven sets of distinct (normalized) lengths ranging from 0.697 to 0.961. Their weighted average, 0.813, nearly coincides with the maximum spectral intensity $F(0.906) \simeq 474$ shown in figure 4. Evidently more refined features of the spectrum encode
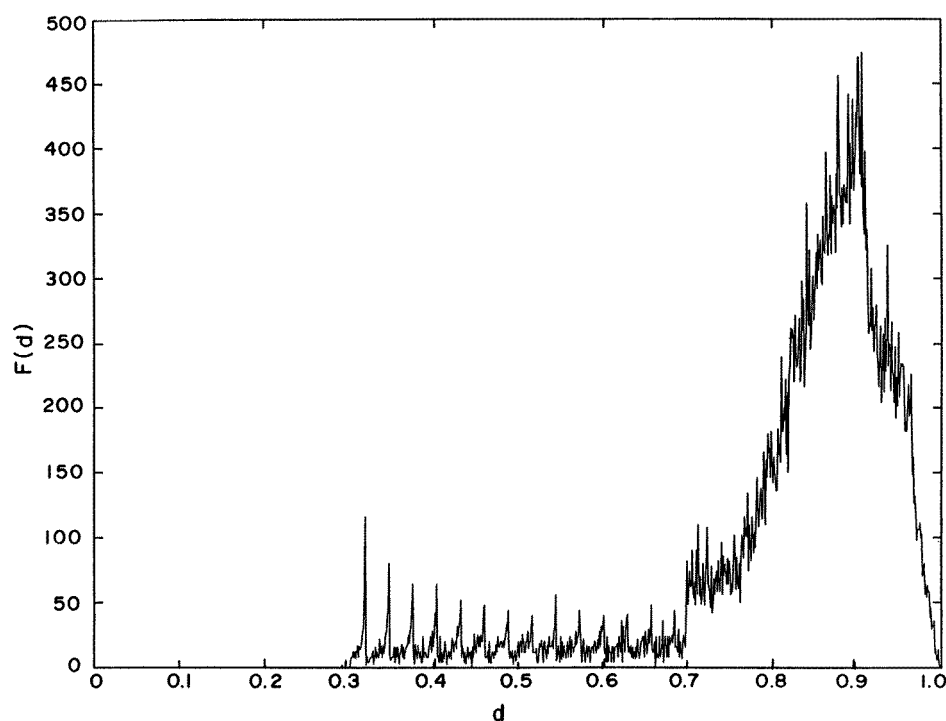
Figure 4. Frequency distribution of the Hausdorff distances between the chiral Coulomb states $C^L(15)$ and $C^R(15)$. In this situation the lower bound of the spectrum is at $d_{min} = 0.291(19)$, and the line spacing is 0.0283. The occurrence of the 'shoulder' at 0.7, and the position of the spectral peak at 0.9 are discussed in the text.

additional information concerning the shapes and relative orientations of $C^L(15)$ and $C^R(15)$. More complicated examples show that this kind of combination of Hausdorff distances and statistics is useful in discriminating among structures that are too complex for conventional symmetry classifications.

5. Saddle point heights and reptation transforms

Since computer trials sampling about 2.3×10^7 relative orientations of $C^L(15)$ and $C^R(15)$ do not lead to any values of the minimum Hausdorff distance lower than that already found for the standard charge positions listed in table 2, the associated Hausdorff matrix in table 3 acquires an additional significance: in this instance, the Hausdorff construction implies that the underlined entries represent a special set of pairings of the ith charges in $C^L(15)$ and the jth charges in $C^R(15)$ with the property that all of their angular separations are minimal. In other words, the maximum overlap between $C^L(15)$ and $C^R(15)$ occurs when they are both in standard orientation, and furthermore, the underlined $i \leftrightarrow j$ pairings in table 3 indicate a minimal set of charge interchanges that convert $C_s^L(15)$ to $C_s^R(15)$ and vice versa. If we now recall that $C_s^L(15)$ and $C_s^R(15)$ also correspond to degenerate minima on an energy surface in a 29-dimensional space, it is plausible that the minimum saddle point height—or activation complex—separating these states of maximum overlap lies along a path of minimal deformation that effects the transformations $C_s^L(15) \leftrightarrow C_s^R(15)$. The analytical version of this construction

is the well known mountain pass theorem [22].

In order to obtain quantitative estimates of the saddle point heights it is, of course, necessary to specify the deformation paths in detail. Since every path actually corresponds to a different transition process, even the constraints implied by the minimum Hausdorff distance constructions still allow for an enormous latitude in the variety of transformations that connect $C_s^L(15)$ to $C_s^R(15)$. Nevertheless, the underlined pairings of charges in table 3 suggests an extremely simple and straightforward procedure for estimating upper bounds for any $C^L(N)$ and $C^R(N)$ couple once their minimum Hausdorff distance orientations have been identified. Let ϕ_i^L, θ_i^L and ϕ_j^R, θ_j^R denote the angular coordinates of the ith and jth charges of $C_s^L(15)$ and $C_s^R(15)$ as specified in table 2. Then assume that in the first approximation the shift from $C_s^L(15)$ to $C_s^R(15)$ is carried out by means of a set of linear transformations

$$\theta_i(s) = \theta_i^L + s(\theta_j^R - \theta_i^L) \tag{20}$$

and

$$\phi_i(s) = \phi_i^L + s(\phi_j^R - \phi_i^L) \tag{21}$$

where the common parameter $0 \leqslant s \leqslant 1$ acts as reaction coordinate, and the $i \leftrightarrow j$ pairings are taken from table 3.

$$
\begin{array}{cccccccccc}
 & i & \leftrightarrow & j & & i & \leftrightarrow & j & & i & \leftrightarrow & j \\
(1) & 4 & & 5 & (5) & 8 & & 9 & (9) & 12 & & 12 \\
(2) & 5 & & 7 & (6) & 9 & & 8 & (10) & 13 & & 10 \\
(3) & 6 & & 4 & (7) & 10 & & 13 & (11) & 14 & & 14 \\
(4) & 7 & & 6 & (8) & 11 & & 15 & (12) & 15 & & 11.
\end{array} \tag{22}
$$

This simple prescription obviously yields a smooth transition from $C_s^L(15)$ to $C_s^R(15)$ as s increases from 0 to 1. If we denote the intermediate configurations by $C^T(s) = C(\phi_i(s), \theta_i(s))$, and $E[C^T(s)]$ is the corresponding Coulomb energy, then evidently [12],

$$E[C_s^L(15)] = E[C^T(0)] \simeq 80.670\,244 \simeq E[C^T(1)] = E[C_s^R(15)] \tag{23}$$

where $\mathrm{Max}[E[C^T(s)]]$, for some $0 < s < 1$, is the saddle point energy *for this particular choice of path*. However, computer trials quickly show that this scheme is not viable because $\mathrm{Max}[E[C^T(s)]] \simeq \mathrm{O}(100)$. This result implies that the saddle point energy is comparable to the average energy of random sets of 15 charges on the unit sphere ($\langle E^{Ran}(15) \rangle = 15^2/2 = 112.5$; cf (3.6) of [12]); or, equivalently, that the saddle point height is of the order of the average altitude of a typical Coulomb 'landscape'. It is easy to check that although each charge position is shifted by only about 10°—which is considerably smaller than the 49° separation between neighbouring charges—the simultaneous movements prescribed by (20) and (21) bring about a transient crowding of charges that results in a significant energy rise.

This is an instructive failure which shows that the coherent movements of complex structures may be impeded by internal energy barriers. Only special kinds of deformations— analogous to the incremental collapse mechanisms of extended frameworks [23]—are energetically favoured. Among these transformations is the extreme option of transferring charges one at a time. Analytically, this is simply done by increasing s from 0 to 1 in the first pair of relations in (20)–(22), while keeping all the other charges fixed. After this transfer is complete, s is increased from 0 to 1 in the next pair (2), thereby moving charge $i = 5$ to the position $j = 7$; these stepwise transfers are then continued until all the charges have been reassembled in $C_s^R(15)$. Computer simulations of this entire set of sequential shifts lead to the surprising result that the maximum intermediate energy is now only 0.2% higher than the chiral endpoint energy 80.670 in (23). Obviously that raises the question of whether still lower saddle point energies might be found by varying the order of the charge transfers in
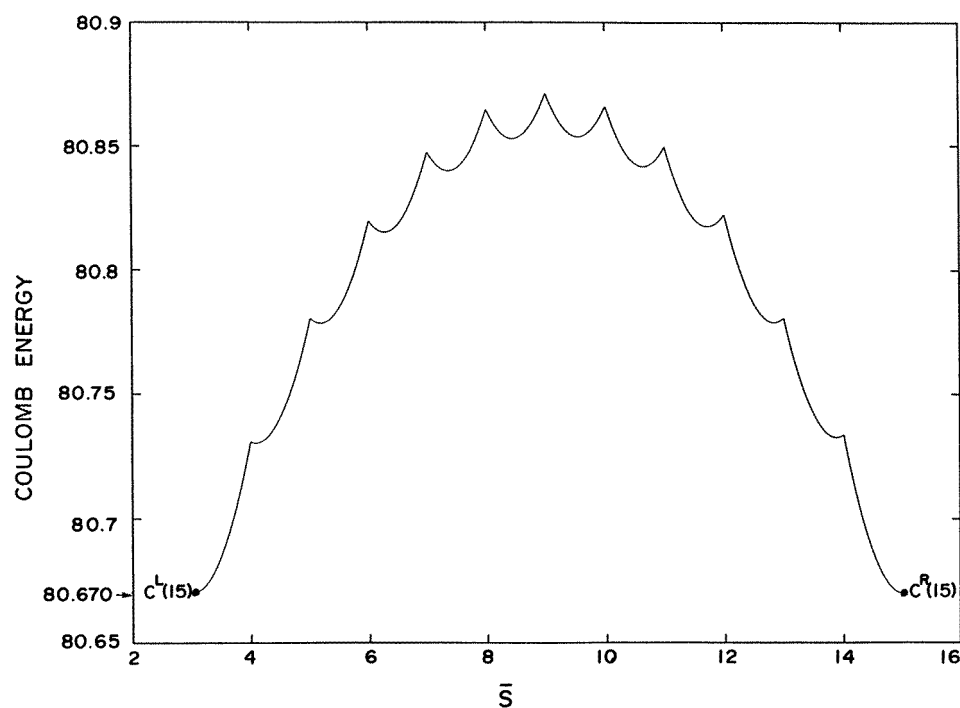
Figure 5. Averaged Coulomb energy profile of 'reptation' transforms between two chiral states. The maximum saddle point height exceeds the $C^{L,R}(15)$ energies by only 0.2%. The scallops correspond to the serial transfer of 12 charges averaged over 2000 sequences randomly chosen from (22). $\bar{s}$ is a generalized reaction coordinate: $3 \leqslant \bar{s} \leqslant 4$ transfers the first charge; $4 \leqslant \bar{s} \leqslant 5$ the second charge, etc.

(20) and (21). Since the pairings in (22) can be rearranged into a total of 12! sequences, it is, of course, impractical to search through all of them; but it is feasible to use pseudo-random number generators to select a sample of 2000 different sets of charge transfers and evaluate the associated energies. Figure 5 shows the resulting averaged energy profiles of these transitions. Again, the average saddle point energy, $\mathrm{Max}\langle E[C^T(s)]\rangle_{2000} \simeq 80.854$, is only about 0.2% higher than the ground state energy. The 12 scallops in figure 5 correspond to the sequential transfers of single charges. As expected, the average energy profile is symmetric about its midpoint, even though the individual charge transfer sequences—which cross different mountain passes between $C_s^L(15)$ and $C_s^R(15)$—generally have asymmetric energy variations.

These results have several broader implications:

(1) In general, searches for the lowest mountain passes on the energy landscapes of complex systems follow along paths of least energy. In the particular case of the Coulomb configurations, the key finding of the computer explorations is that sequential charge movements occur with lower energy variations than collective displacements mediated by (20) and (21). If this trend can be extrapolated to much more complex systems it may be a contributing factor to the occurrence of reptation in polymer dynamics.

(2) The estimate that $C_s^L(15)$ and $C_s^R(15)$ are separated by a saddle point whose energy is only 0.2% higher than the ground state energies, implies that these states are joined by at least one 'reaction pathway' that follows along a nearly flat valley bottom on the energy landscape. A still lower mountain pass route with an energy increment of only 0.002%
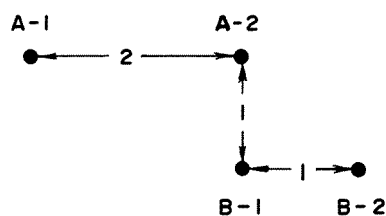
Figure 6. Hausdorff metric constructions for two sets, *A* and *B*, each consisting of two points. The distances are displayed in table 6.

has recently been found by Toomre [24]. Both of these results clearly show that although $C_s^L(15)$ and $C_s^R(15)$ are sharply differentiated by chiral symmetry, the interconversion of $C_s^L(15) \leftrightarrow C_s^R(15)$ is barely inhibited by energy barriers. This rudimentary model may be related to the spontaneous racemization that occurs in some amino acids. It is well known that the L-amino acids (L = levorotatory) commonly found in living systems are the result of the stereochemical specificity of enzymes that utilize only the L-enantiomers [25]. However, the L-aspartic acid in human tooth enamel converts into the D-aspartic enantiomer at a nearly constant rate of about 0.1% per year. This provides a chiral marker for determining human biological age [25–27].

(3) The local energy minima of many cooperative systems—including the Coulomb configurations and simple protein models—are nearly all degenerate. This implies that the associated energy landscapes are bounded below by a single hyperplane that is approximately tangent to every local minimum. Consequently, the minimum energies have no direct relation to the size of the capture basins or probabilities of occurrence of particular states (Levinthal's paradox [28]). These degeneracies are regarded as essential in some complex organic molecules because otherwise evolution would have simply minimized energy rather than optimize functionality and fitness [29]. Comparisons of the energy profiles of the 2000 $C_s^L(15) \leftrightarrow C_s^R(15)$ transitions show that this pervasive degeneracy can extend from states to processes: all of these transformations flow through a narrow energy band limited by the maximum and minimum saddle point heights, i.e. $80.9469 - 80.7878 \simeq 0.16$. Levinthal's paradox re-emerges at this level because alterations in the order of the charge transfers have negligible influence on the energy variations.

6. Asymmetric Hausdorff distances and parity

The origin of asymmetries in the Hausdorff distances between sets is illustrated by the simple example of figure 6. Obviously, the smallest disc centred at the points *B*-1 and *B*-2, that includes at least one point of the set *A*, has radius $\sqrt{2}$: in contrast, the smallest disc centred at *A*-1 and *A*-2, that includes at least one point of the set *B*, has radius $\sqrt{5}$. Table 6 which is a mini-version of (2), together with (3)–(5), then shows that the corresponding set of Hausdorff distances is given by

$$\delta(A \to B) = \sqrt{5} \qquad \delta(B \to A) = \sqrt{2} \tag{24}$$

and

$$\delta(A, B) = \sqrt{5}. \tag{25}$$

In general, these distances depend both on the configurations as well as the relative positions of the sets. But if we specialize *A* to represent a finite set of points on the surface of a sphere, and *B* is another set obtained by reflecting *A* in a great circle, followed by rotation

Table 6. Euclidean and Hausdorff distances between the point sets A and B in figure 6.

	B-1	B-2	Minimum by rows	Max–min by rows
A-1	$\sqrt{5}$	$\sqrt{10}$	$\sqrt{5}$	$\sqrt{5} \to \delta(A \to B)$
A-2	1	$\sqrt{2}$	1	
Minimum by columns	1	$\sqrt{2}$		
Max–min by columns	$\sqrt{2} \to \delta(B \to A)$			
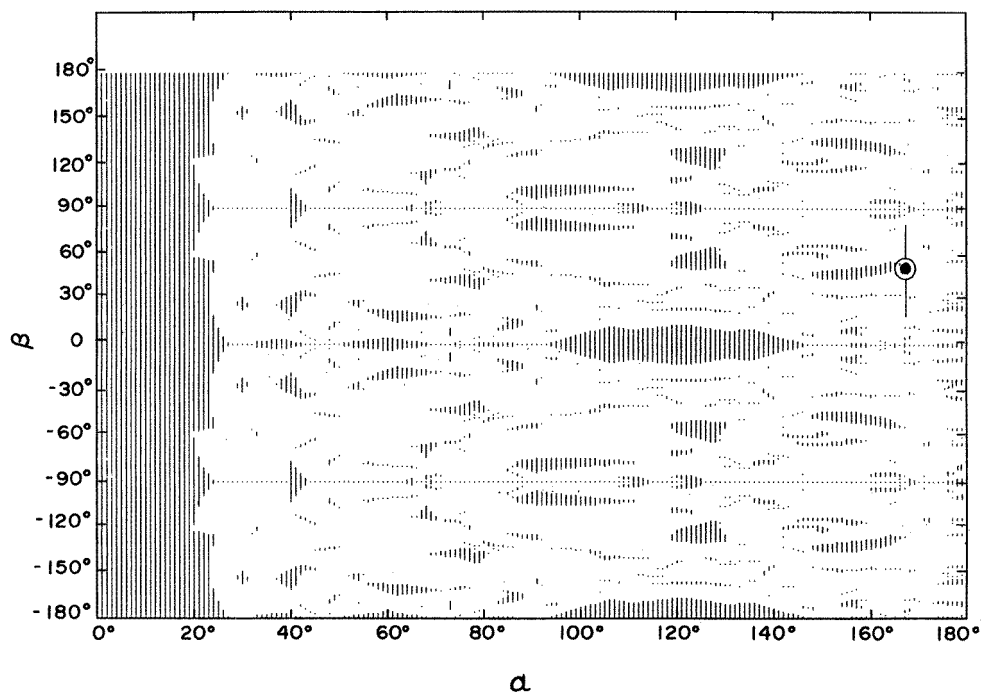
Figure 7. Hausdorff distances between two rotated chiral states $C_s^L(15)$ and $C_{\alpha,\beta}^R(15)$. The shaded zones indicate relative orientations with symmetric Hausdorff distances. The bull's eye at $\alpha = 168°$, $\beta = 57°$ corresponds to an orientation with maximally asymmetric distances.

about a point on that same circle, then the Hausdorff distances between A and B are necessarily symmetric [30]. Since these rotatory reflections include chiral pairs of Coulomb states, this lemma accounts for the symmetry of the Hausdorff distances between $C_s^L(15)$ and $C_s^R(15)$ found previously in (15) and (16).

These constraints do not apply to the more general transformations such as the tilts and rotations utilized in section 4 in the search for minimum Hausdorff distances. To be specific, let $C_{\alpha,\beta}^R(15)$ represent the $C_s^R(15)$ configuration after it has been isometrically shifted so that its 'north pole' charge is at colatitude α longitude β. By recomputing the associated Hausdorff matrix (2) for every value of α and β, it is possible to compare the two distances $\delta(C_s^L(15) \to C_{\alpha,\beta}^R(15))$ and $\delta(C_{\alpha,\beta}^R(15)) \to C_s^L(15))$. These results are summarized in figure 7. The shaded zones in the α–β plane—which cover about 25% of the total area—indicate relative orientations of $C_s^L(15)$ and $C_{\alpha,\beta}^R(15)$ with symmetric Hausdorff distances:

the remaining blank spaces correspond to asymmetric distances. Some features of these zone patterns are intuitively plausible. For instance, since $C_{0,\beta}^R(15)$ coincides with $C_s^R(15)$, the equality of the distances in (15) and (16) shows that $\alpha = 0$ must be the boundary of the shaded zone. Continuity implies that this zone extends at least as far as $\alpha \simeq O(10°)$ because this is the minimum (non-vanishing) angular separation between the charges in $C_s^R(15)$ and $C_s^L(15)$. The bull's eye at $\alpha = 168°$ and $\beta = 57°$ indicates a relative orientation where the directed Hausdorff distances between the chiral pairs are maximally different, i.e.

$$d(C_s^L(15) \to C_{168°,57°}^R(15)) = 0.779 < 0.968 = d(C_{168°,57°}^R(15) \to C_s^L(15)). \qquad (26)$$

Equation (26) effectively says that $C_s^L(15)$ is a better fit to $C_{168°,57°}^R(15)$ than the other way around, even though the intrinsic structures of both states are simply related by rotatory reflections. This result is another illustration of the general principle that increasing complexity is correlated with symmetry breaking. Several clear examples are provided by the surface Coulomb states: for instance, the dipole moments of all the equilibrium configurations $C(N), 2 \leqslant N < 11$ vanish in apparent harmony with general parity arguments [31], but, beginning with $C(11)$, states with finite moments occur with increasing frequency. Similarly, despite the spherical symmetries of the Coulomb interaction and the boundary conditions, chiral solutions that 'spontaneously' break rotational symmetry first appear at $N = 15$. The symmetry breaking in (26) is qualitatively different because complexity in this situation arises from a particular algorithm, or process, that links the two states. If the separation between $C_s^L(15)$ and $C_{\alpha,\beta}^R(15)$ were measured by the Euclidean distance between sets [32], rather than the Hausdorff distance, there would be no asymmetries. A physical parallel is the conservation of parity in strong interactions and the breaking of this symmetry by weak interactions.

Of course, global symmetries can occasionally be restored by appealing to statistical balance: the dipole moment of $C(11)$ can point in any direction; each of the two chiral states $C^L(15)$ and $C^R(15)$ occurs with 50% frequency; and the obvious symmetries of the zone patterns about $\beta = 0°$ in figure 7 show that there are complementary set orientations where the inequality in (26) is reversed. But these arguments in turn are merely circular consequences of the 'principle of insufficient reason' [33], and it is easy to construct counter-examples [12]. There is, in fact, a lengthy history of fallacies and contradictory conclusions which shows that this 'principle' is too vague to be useful for the foundations of probability and decision theory [33].

7. Speculative extensions

The computer explorations in section 5 were carried far enough to verify that the Hausdorff metric could be used as an aid to locate saddle points on the energy surfaces of the spherical Coulomb problem. If a sufficient number of these saddle points could be found, crude estimates of the relative sizes of various capture basins would be feasible, and the results correlated with the available statistics on the associated frequencies of occurrence [12]. Model studies suggest that some complex gradient systems preferentially evolve towards a small subset of energy minima because these minima are surrounded by large capture basins. This topographic bias is presumed to be the accelerated selection mechanism that bypasses Levinthal's paradox [34]. The next step is to identify the structural characteristics that permit the maximum crowding of states with the least energy cost in these favoured basins. Since the Hausdorff distance is a natural measure of the resemblance, or nearness, of configurations, it seems reasonable to include this information by superposing a Hausdorff metric on the energy landscapes.

The symmetry breaking inherent in the formation of chiral states and dipole moments is the basis for many physical effects such as optical rotation and piezoelectricity. It is interesting

Table 7. Partial Coulomb interaction energies (27) and (28), for the chiral states $C_s^L(15)$, $C_{168°,57°}^R(15)$.

i	1	2	3	4	5	6	7	8	9	10	11	12	13	14	15
E_i[a]	5.11	4.47	3.94	3.58	4.09	4.84	3.64	3.97	3.94	4.06	4.11	3.63	3.50	3.57	3.58
E_j[a]	4.39	3.75	3.72	3.53	4.25	3.80	4.17	4.31	3.74	3.77	4.02	4.90	3.21	4.80	3.68
j	1	2	3	4	5	6	7	8	9	10	11	12	13	14	15

[a] Add 10 to every entry to obtain the actual value.

to speculate whether the extreme asymmetry expressed by the differences of the Hausdorff distances in (26) might also have some consequences for 'real world' physics. One tangible link is the Coulomb energy of the individual charges in a configuration [35]. Columns 4 and 8 in table 2 show how the total Coulomb energy ($\simeq 80.670$) of the $C^{L,R}(15)$ states is apportioned among the various charges. Obviously the distribution of these partial energies is the same for both enantiomers, and is also preserved for all isometric transformations of each configuration. However, this symmetry does not extend to the mutual Coulomb energies of the chiral states. Let ψ_{ij} denote the angular separation between the ith charge in $C_s^L(15)$ and the jth charge of the tilted configuration $C_{168°,57°}^R(15)$, cf (1). The interaction energy then is $\frac{1}{2}\csc(\Psi_{ij}/2)$, and consequently

$$E_i = \tfrac{1}{2}\Sigma_j \csc(\Psi_{ij}/2) \tag{27}$$

is the partial Coulomb energy of the ith charge due to its interaction with all the charges in $C_{168°,57°}^R(15)$. Similarly

$$E_j = \tfrac{1}{2}\Sigma_i \csc(\Psi_{ij}/2) \tag{28}$$

is the partial energy of the jth charge due to its interaction with all the charges in $C_s^L(15)$. Since the basic Hausdorff matrix (2) for these relative orientations has already been computed for (26), it is straightforward to obtain the distribution of partial energies. The essential result, which is apparent from table 7, is that none of the entries for E_i and E_j match. This implies that the Coulomb energy environment and the internal forces of the two chiral states are completely different (diastereoisomerism), although the total interaction energies and forces balance, e.g. $\Sigma_i E_i = \Sigma_j E_j \cong 210$.

The correlations between symmetry breaking and complexity are also related to the deeper question of whether all the information contained in functions of n (>2) variables can be completely encoded by the superposition of functions of fewer variables. Precise mathematical formulations of these issues stem from Hilbert's 13th problem [36]. The principal conclusions of these studies are twofold: (i) continuous functions of n (>2) variables can generally be represented by finite combinations of continuous functions of one and two variables; but (ii) if further degrees of smoothness—such as continuous differentiability—are imposed, then it is possible to prove the existence of intrinsically irreducible n-place functions [36]. Since the zone boundaries in figure 7 mark breaks in the continuous differentiability of the Hausdorff distances, it is plausible that the irreducibility results of (ii) may be relevant. In these cases the Hausdorff distances could be associated with collective forces—analogous to exchange forces—that incorporate more information than is contained in the underlying Coulomb interactions [37].
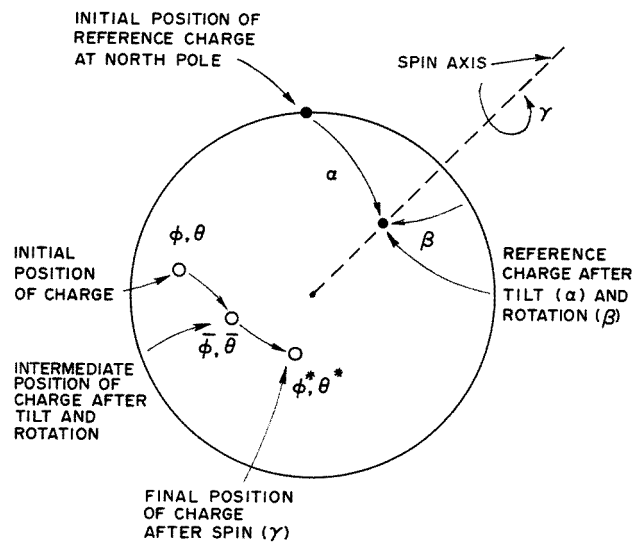
Acknowledgments

Figure 8. Rotations of Coulomb configurations. The full circles show the movement of the reference charge; the open circles show the associated movement of the ith charge.

discussions and orientations to the literature.

Appendix. Rotations of Coulomb configurations

Let $C(\vec{r}_i(\phi_i, \theta_i))$, $1 \leqslant i \leqslant N$, denote a Coulomb state specified by a set of radial vectors, $|\vec{r}_i| = 1$, that locate the N point charges on the surface of the unit sphere. The angular positions of the charges are given by the colatitudes ϕ, $0 \leqslant \phi \leqslant \pi$, and longitudes θ, $-\pi \leqslant \theta \leqslant \pi$. Initially, the C states are oriented so that a charge—called the reference charge—is located at the north pole, $\phi = 0$ [12]. If the reference charge is moved to colatitude α and longitude β—as shown in figure 8—a rigid tilting and rotation of the C-state to the new orientation $C_{\alpha,\beta}$ will move the ith charge from ϕ_i, θ_i to $\bar{\phi}_i, \bar{\theta}_i$. The new angular coordinates are given by

$$\bar{\phi} = \cos^{-1}[\cos\alpha \cos\phi - \sin\alpha \sin\phi \cos(\theta - \beta)]. \tag{29}$$

Furthermore

$$\sin(\bar{\theta} - \beta) = \sin(\theta - \beta) \sin\phi / \sin\bar{\phi} \tag{30}$$

and

$$\cos(\bar{\theta} - \beta) = [\cos\phi - \cos\bar{\phi} \cos\alpha]/ \sin\bar{\phi} \sin\alpha. \tag{31}$$

Since $-\pi \leqslant \bar{\theta} \leqslant \pi$, both (30) and (31) are required to fix the value of $\bar{\theta}$. (For simplicity, the subscript i is omitted in equations (29)–(37)). If a charge initially happens to be at colatitude $\alpha(\phi = \alpha)$, and is on the same meridian as the reference charge ($\theta = \beta + \pi$), its new position will coincide with the north pole, $\bar{\phi} = 0$. In these cases, the analytical indeterminacy of (30) and (31) reflects the fact that the longitude is not defined at the pole. Allowance for this contingency has to be included in the computer routines.

The remaining 'spin' degree of freedom is represented by a rotation through an angle γ, $0 \leqslant \gamma \leqslant 2\pi$, about an axis passing through the reference charge at α, β, and the centre of the sphere. As indicated in figure 8, this spin results in a further movement of the ith

charge from the intermediate coordinates $\bar{\phi}_i$, $\bar{\theta}_i$, to its final position at ϕ_i^*, θ_i^*. The associated computations can be expressed concisely in terms of two auxiliary angles, $0 \leqslant \xi \leqslant \pi$ and $0 \leqslant \gamma' \leqslant 2\pi$, given by

$$\xi = \cos^{-1}[\cos\alpha\cos\bar{\phi} + \sin\alpha\sin\bar{\phi}\cos(\bar{\theta} - \beta)] \tag{32}$$

and

$$\sin(\gamma + \gamma') = \sin(\bar{\theta} - \beta)\sin\bar{\phi}/\sin\xi \tag{33}$$

$$\cos(\gamma + \gamma') = [\cos\bar{\phi} - \cos\alpha\cos\xi]/\sin\alpha\sin\xi. \tag{34}$$

In parallel with (30) and (31), both (33) and (34) are required to find the value of γ' corresponding to a particular choice of γ. Finally,

$$\phi^* = \cos^{-1}[\cos\alpha\cos\xi + \sin\alpha\sin\xi\cos\gamma'] \tag{35}$$

and

$$\sin(\theta^* - \beta) = \sin\xi\sin\gamma'/\sin\phi^* \tag{36}$$

$$\cos(\theta^* - \beta) = [\cos\xi - \cos\alpha\cos\phi^*]/\sin\alpha\sin\phi^*. \tag{37}$$

In practice, the invariance of the partial Coulomb energies of all the charges is checked after every rotation.

References

[1] Wu C S 1959 *Rev. Mod. Phys.* **31** 783–90
[2] Leutwyler H 1995 *Chiral Dynamics: Theory and Experiment* ed A M Bernstein and B R Holstein (New York: Springer) pp 14–29
[3] Pasteur L 1848 *Ann. Chim. Phys.* **24** 442–60
Pasteur L 1850 *Ann. Chim. Phys.* **28** 56–99
Pasteur L 1853 *Ann. Chim. Phys.* **38** 437–83
[4] Guye P-A 1890 *C. R. Acad. Sci., Paris* **110** 714
[5] Tinoco I and Woody R W 1964 *J. Chem. Phys.* **40** 160–5
[6] Buda A B, auf der Heyde T P E and Mislow K 1991 *J. Math. Chem.* **6** 243–53
[7] auf der Heyde T P E, Buda A B and Mislow K 1991 *J. Math. Chem.* **6** 255–65
[8] Weinberg N and Mislow K 1993 *J. Math. Chem.* **14** 427–50
[9] Weinberg N and Mislow K 1995 *J. Math. Chem.* **17** 35–53
[10] Buda A B, auf der Heyde T and Mislow K 1992 *Angew. Chem. Int. Ed. Engl.* **31** 989–1007
[11] Erber T and Hockney G M 1991 *J. Phys. A: Math. Gen.* **24** L1369–77
[12] Erber T and Hockney G M 1997 *Adv. Chem. Phys.* vol 98, ed I Prigogine and S A Rice (New York: Wiley) pp 495–594
[13] Johnson N W 1966 *Can. J. Math.* **18** 169–200
[14] Bijvoet J M, Peerdeman A F and van Bommel A J 1951 *Nature* **168** 272
[15] Weyl H 1952 *Symmetry* (Princeton, NJ: Princeton University Press)
[16] Hausdorff F 1927 *Mengenlehre* (Berlin: de Gruyter)
[17] Fréchet M 1906 *Rend. Circ. Mat. Palermo* **22** 1–74
[18] Andreev N N 1996 *East J. Approx.* **2** 459–62
[19] Edmundson J R 1992 *Acta Crystallogr.* A **48** 60–9
[20] Klein F 1913 *Lectures on the Icosahedron* (London: Kegan Paul)
[21] Conway J H, Curtis R T, Norton S P, Parker R A and Wilson R A 1985 *Atlas of Finite Groups* (Oxford: Clarendon)
[22] Ambrosetti A and Rabinowitz P H 1973 *J. Funct. Anal.* **14** 349–81
[23] Guralnick S A, Erber T, Soudan O and Stefanis J 1988 *J. Struct. Engng* **114** 31–49
[24] Toomre A Private communication
[25] Helfman P M and Bada J L 1975 *Proc. Natl Acad. Sci. USA* **72** 2891–4
[26] Hayflick L 1994 *How and Why We Age* (New York: Ballantine)
[27] Mornstad H, Pfeiffer H and Teivens A 1994 *J. Forensic Sci.* **39** 1425–31
[28] Frauenfelder H and Wolynes P G 1994 *Phys. Today* **47** 58–64
[29] Grosberg A Yu and Khokhlov A R 1997 *Giant Molecules* (San Diego, CA: Academic)

[30] Frank M J Private communication
[31] Wigner E 1927 *Z. Phys.* **43** 624–52
[32] Zong C 1996 *Strange Phenomena in Convex and Discrete Geometry* (New York: Springer)
[33] Keynes J M 1957 *A Treatise on Probability* (London: Macmillan)
[34] Doye J P K and Wales D J 1998 *Phys. Rev. Lett.* **80** 1357–61
[35] Claxton T A and Benson G C 1966 *Can. J. Chem.* **44** 157–63
[36] Lorentz G G 1976 *Mathematical Developments Arising from Hilbert Problems (Proc. Symp. Pure Math. 28)* ed
         F E Browder (Providence, RI: American Mathematical Society) pp 419–30
[37] Present R D 1971 *Contemp. Phys.* **12** 595–602